

# Photodimerization Induced Hierarchical and Asymmetric Iontronic Micropatterns

**Zehong Wang**

Shanghai Jiao Tong University

**Tiantian Li**

Shanghai Jiao Tong University <https://orcid.org/0000-0001-6828-5637>

**Yixiang Chen**

Donghua University

**Jin Li**

Shanghai Jiao Tong University

**Xiaodong Ma**

Shanghai Jiao Tong University

**Jie Yin**

Shanghai Jiao Tong University

**Xuesong Jiang** (✉ [ponygle@sjtu.edu.cn](mailto:ponygle@sjtu.edu.cn))

Shanghai Jiao Tong University <https://orcid.org/0000-0002-8976-8491>

---

## Article

### Keywords:

**Posted Date:** July 6th, 2022

**DOI:** <https://doi.org/10.21203/rs.3.rs-1779769/v1>

**License:**  This work is licensed under a Creative Commons Attribution 4.0 International License.

[Read Full License](#)

---

**Version of Record:** A version of this preprint was published at Nature Communications on October 30th, 2022. See the published version at <https://doi.org/10.1038/s41467-022-34285-7>.

# Abstract

Micropatterning various ions-based modality materials offers compelling advantages for their functionality enhancement in iontronic pressure sensing, piezoionic mechanoreception, and skin-interfaced electrode adhesion. However, most existing patterning techniques for iontronic materials suffer from low flexibility and limited modulation capability. Herein, we propose a facile and robust method to fabricate hierarchical and asymmetrical iontronic micropatterns (denoted as HAIM) through programmed regulation of the internal stress distribution and the local ionic migration among an iontronic host. The resultant primary patterns and secondary wrinkles with arbitrary regulated morphology and region-dependent ionic electrical performance can be readily made upon iontronic host via localized photodimerization of anthracene-functionalized ionic liquid copolymer (denoted as An-PIL) and subsequently vapor oxidative polymerization of 3,4-ethylenedioxythiophene (EDOT). By controlling the local secretion of room temperature ionic liquid (denoted as IL) droplets and subsequently doping into the resultant PEDOT, it was possible to modulate the surface conductivity as well as the potential gradients of the HAIM. Taking the spatiotemporal advantages of light, heat, and vapor, the morphology and electrical performance of HAIM can be modulated by programmed exposure with photomask and polymerization time. Besides, based on the piezoionic effect within the resultant IL-doped PEDOT, the HAIM can serve as a scalable iontronic potential generator. The successful synthesis of these fascinating micropatterns may provide new insights into the development of patterned iontronic materials in a flexible, programmable, and functionally adaptive form.

## 1 Introduction

Hierarchical micro-nano patterns enable biological surfaces to exhibit diverse properties and functions, such as antireflection, drag reduction, anti-adhesion, power generation, environment sensing, etc.<sup>1, 2, 3, 4</sup>. Among them, the various sensitively tactile perception is attractive and caused by the collaboration systems between hierarchical microstructures and heterogeneous component molecules of the patterned biological surfaces<sup>5, 6</sup>. For example, the sensation of fingertip is owing to ) the conformal wrinkles on fingerprint can effectively transmit external stimulus to the subcutaneous receptors<sup>7</sup>; ) the established transmembrane potential caused by the asymmetric bilayer lipids inside and outside the cell membrane can promote stable and fast mechanotransduction<sup>8, 9</sup>. Inspired by the bioelectronics mechanisms of biological surfaces, many artificial iontronic hosts have been developed and applied in spontaneous power generation<sup>10</sup>, highly sensitive pressure sensor<sup>11</sup>, electrochemiluminescence devices<sup>12</sup>, and ionic heterojunction interface<sup>13</sup>. Nevertheless, most of them are prepared from structural engineering techniques, i.e. photolithography, nanoimprinting, template transferring, and layer-by-layer deposition are utilized to construct hierarchical topographies (such as pyramids, cracks, wrinkles, and domes) or asymmetric iontronic interfaces<sup>14, 15, 16, 17, 18</sup>. Despite complicated surface patterns can be fabricated by top-down techniques with precisely control<sup>19</sup>, however, most of them involve lengthy and complex fabrication processes<sup>20, 21</sup>. Moreover, the resultant patterns are fixed, difficult to dynamically regulate, and do not conformal to the bioelectronics modality that through controlling the flow, regions, and

concentrations of ionic charge to interface with the environment<sup>22</sup>. More effective, easy-to-process, programming-controllable, and dynamically adaptable methods to manipulate ionic electrical performance for iontronic materials are needed.

In contrast to traditional top-down approaches, biological surface patterns that evolve from nature are usually spontaneous and self-organized, and generally involve the transfer of matter or energy and the interaction of compressive stress<sup>23, 24, 25, 26</sup>. Among them, self-wrinkling is the most common pattern of living organisms and regulated by the compressive forces originating from gradients in stress normal to the surface or mismatches in properties between different layers of skins<sup>27, 28</sup>. On this basis, self-wrinkling can introduce onto the surface of iontronic materials, and then the internal stress distribution can be varied by external stimulus to simultaneously achieve dynamic regulation of the surface topography and internal ionic charge distribution, thereby establishing hierarchical and heterogeneous iontronic surface. Photoinduced cross-linkable poly (ionic liquid) (denote as PIL), as the forefront of advanced and versatile iontronic materials, have high ionic conductivity, good processability, substantial amount of mobile cations and anions, and high compatibility with small polar compounds<sup>29, 30</sup>. These materials would be, in this regard, a great promise as an exceptional candidate for constructing hierarchical iontronic patterns. However, since the mobile ions in homogeneous PIL can only migrate and redistribute in a small region along with the polymer chains before and after photocrosslinking, thus it is difficult to dramatically vary the ionic electrical performance for the surface patterns to the need. Alternatively, developing a heterogeneous PIL system that can synchronously control the morphology of iontronic patterns and greatly change the ions concentration along with different cross-linked regions will be more promising.

According to our previous work, surface wrinkling can dynamically and precisely regulate and arbitrarily tune topographies of surface in two dimensions<sup>31</sup>. Herein, we present a robust method to create hierarchical and asymmetric iontronic micropatterns (denoted as HAIM) by incorporating masked photodimerization and asymmetric vapor oxidative polymerization that supported by an in-situ phase separation process. A random copolymer comprised of two groups (anthracene-functionalized ionic liquid and n-butyl acrylate) (denoted as An-PIL) with distinct solubility in 1-ethyl-3-methylimidazolium bis(trifluoromethylsulfonyl)imide (denoted as IL) was prepared to achieve the aim of accumulating the internal stress under UV exposure and readily regulating stress distribution to produce self-wrinkling patterns under a mask. Moreover, an inhomogeneous iontronic host comprise of An-PIL and IL was developed to realize the goal of in-situ phase separation and thus vary the mobile ionic species among different patterned regions and also support the vapor oxidative polymerization. The strategy combined the advantages of the top-down method (precise and controllable), self-organized wrinkling (simple and natural), and bioelectronics mechanisms (tunable ionic charge and action potential), paving a way for simple, controllable, and operable manufacturing of organic electronics. The resultant HAIM exhibits integrated properties of highly polarizable PIL, ease of mobile ionic charge, capacitive and potentiometric gradient controllability, and long-term durability. The incorporation of photodimerization to fabricate HAIM was demonstrated to achieve promising bioelectronics modality either on macro or micro scales.

## 2 Results And Discussion

### 2.1 Synthesis and ionic electrical modality of HAIM

We prepared the HAIM based on three criteria: (i) the iontronic host can effectively crosslink via anthracene group under UV exposure, (ii) the iontronic host must be able to store ionic charges and readily redistribute them under the external stimulations, and (iii) the iontronic host must further processing to construct hierarchical and asymmetric patterns through controllable gas phase polymerization. The first two requirements were satisfied by developing An-PIL/IL mixture with minimal free energy, among which An-PIL was used as photodimerization functional matrices to generate micropatterns and microstructures<sup>28</sup>, and liquid IL with a substantial amount of mobile ionic charge acted as a migrant phase to realize the ionic redistribution. To satisfy the last criterion, vapor oxidative polymerization of 3,4-Ethylenedioxythiophene (EDOT) was carried out under a non-uniform chemical environment, and the resultant hierarchical morphology and asymmetrical iontronic performance came from the twice regulation of internal stress as well as distinct IL-doped PEDOT synthesized upon exposure and unexposed regions.

Figure 1A describes the overall chemical reactions and synthesized molecular structures. A random copolymer An-PIL was synthesized to bring about the photocrosslinking for iontronic host. Moreover, IL was used as a plasticizer and separable moieties to vary the glass transition temperature ( $T_g$ ) of An-PIL and provide microreactor for the synthesis of IL-doped PEDOT. The synthesis and characteristics of An-PIL was provided in Figure S1 and Figure S2. The fabrication process began with the preparation of An-PIL/IL film (i.e. iontronic host) comprise of different molar ratios of IL to the anthracene unit of An-PIL. Subsequently, the iontronic host became highly miscible and well dispersive with the help of the resemble structure and close characters between IL and An-PIL backbones (i.e. the solubility parameter close principle<sup>32</sup>). Thereafter, primary patterns were generated by localized photodimerization of iontronic host with photomasks and that can be understood as the self-wrinkling appeared at the exposure region due to the gradient photocrosslinking (Fig. 1B). In addition, after heating treatment at 85°C for 15 min, the IL droplets was secreted from iontronic host and firmly adhered to primary patterns. Notably, the IL droplets secretion only occurs in exposure region (i.e. primary patterns) and which can be washed out by ethanol, as shown in Figure S3. To further build hierarchical micropatterns onto the iontronic host, vapor oxidative polymerization of EDOT was conducted and resulting in secondary wrinkles formation onto previous unexposed regions. Meanwhile, the IL droplets on primary patterns acted as a microreactor to produce IL-doped PEDOT while pure PEDOT was synthesized on the surface of secondary wrinkles. As a result of formation of asymmetrical iontronic micropatterns. Figure 1C shows the optical images of a typical HAIM with a hierarchical surface containing stripe patterns (i.e. primary patterns) and random wrinkles (secondary wrinkles). The representative field-emission scanning electron microscopy (FE-SEM) image of the relevant surface morphology presented in Fig. 1D and Fig. 1E revealed that spherical IL-doped PEDOT with diameters of  $\sim 5 \mu\text{m}$  was aggregated onto primary patterns while flaky pure PEDOT are widely distributed onto secondary wrinkle.

Figure 1F demonstrates the proposed mechanisms for the ionic migration behavior of HAIM against external compressions. Owing to the presence of mobile ionic charges in IL-doped PEDOT and once HAIM were squeezed, the mobile ionic charges will be depolarized and compelled to spatially redistribute within the scaffolding polymer matrix, which we refer to as the piezoionic effect<sup>33, 34, 35</sup>. Moreover, since there is a difference between the transport capability of the ionic charges in the PEDOT/IL-rich domain in response to the built stress distribution, i.e. the cations in IL is positively charged and the interactions between cations and the main chain of PEDOT is weaker, thus, it is easier for cations to move to the opposite side away from the external force. Meanwhile, due to the stronger electrostatic force between anions ( $I^-$  and  $TFSI^-$ ) and the positive charged PEDOT, the anions will be remained relatively near the surface. Ultimately, a negative space charge near the interface of the external force and a positive space charge at the interface far from the external force were generated, respectively. In addition, since there were no excess mobile ionic charges in pure PEDOT on secondary wrinkles and it will exhibit electrically neutral under the action of external force. Therefore, based on the distinct piezo-ionic effect of hierarchical iontronic micropatterns, the resultant HAIM exhibit asymmetrical ionic electrical performance and potential gradient under the action of an external force when connected to an external circuit.

## 2.2 Photodimerization and phase separation of iontronic host

To clarify the mechanism of photodimerization inducing subsequent phase separation for iontronic host, we conducted a series of controlled experiments and used the corresponding IL molar ratios-dependent micropatterns' morphology variation to determine the factors for the initial photocrosslinking event and the resultant IL droplets secretion. The iontronic host comprise of different molar ratios of An-PIL to IL were exposed on UV light with a photomask to achieve local photodimerization, and then heated to achieve the secretion of IL droplets onto the primary patterns (Fig. 2A-C). As the molar ratios of An-PIL to IL increased, the amplitude (i.e. the height) of the resultant primary patterns was grown from 0  $\mu\text{m}$  (the molar ratio of An-PIL to IL was 1:0, i.e. 0%) to 20  $\mu\text{m}$  (the molar ratio of An-PIL to IL was 1:10, i.e. 91%), as shown in Fig. 2D. Subsequently, after heating the obtained primary patterns at 85°C for 15 min, IL droplets began to secrete from the surface of primary patterns when the molar ratios of An-PIL to IL was 1:1 (i.e. 50%), as shown in Figure S4. Moreover, the diameters of IL droplets were reduced from 19.7  $\mu\text{m}$  to 12.9  $\mu\text{m}$  until finally disappeared as the molar ratios of IL further increased. Remarkably, the as-prepared primary pattern (corresponding to the exposure region) has a clear boundary (Fig. 2B), and the IL droplets had been confined to the boundary of the primary pattern.

To gain insight into the mechanism for IL droplet secretion, we investigated the LSCM image and the corresponding phase images of a representative primary pattern in Fig. 2B. In order to better illustrate the internal phase structure change of the iontronic host, we divided the resultant surface patterns into three parts: I represent the unexposed region (i.e. the pristine iontronic host), II represent the transition region between the unexposed region and exposure region, and III represent the exposure region (i.e. IL droplets @primary patterns), as shown in Fig. 2E-F. The LSCM image in Fig. 2F shows that evenly spaced stripe

patterns were covered by IL droplets, whereas the transition region and unexposed region are flat and have no obvious change. Besides, the phase image of the unexposed region (Fig. 2G) shows a distinct nanophase-separated structure in the region I. Based on the microphase separation in the unexposed region and according to the like dissolves like rule, we proposed that the weak polarity of BA segments drives aggregation to form phase-separated BA-rich domains, on the contrary, the strong polarity of An-IL enables the An-IL-rich domains to be surrounded by IL, as shown in Fig. 2J. Meanwhile, the brighter region in the phase image (Fig. 2G) corresponds to the hard region (i.e. the An-IL moiety), and the darker region corresponds to the soft segment (i.e. the BA unit). After localized photodimerization and heating to secrete IL droplets, a relatively uniform miscible phase structure was formed in region (Fig. 2I). Moreover, although the transition region (II) is unexposed, however, its phase image distribution appears more uniform than that of the pristine unexposed region (I). Therefore, the mobile IL phase may migrate from the transition region to the exposure region and thus enable the An-IL and BA segment units in region II to become more homogenous.

To investigate the role of heating on IL phase separation, we heated the photodimerization cross-linked patterns (among which the molar ratios of An-PIL to IL were 1:2) at 85°C and analyzed the diameter variation of IL droplets as a function of heating time, as shown in Fig. 2K. As the heating time increased, the diameter and height of IL droplets increased from 0 μm (0 min) to 17.6 μm and 2.5 μm (12 min), respectively, and then slightly decreased until unchanged. Based on the above results, we propose that the initial mixing of An-PIL dimer and IL is thermodynamically unstable, and IL tends to phase separate and readily aggregate each other into larger droplets after heating. Moreover, since An-IL segments have good compatibility with IL with the help of the ionization of the imidazolium group and hydrogen bond interaction, therefore a miscible and stable iontronic host could be formed initially (Figure S5). Meanwhile, due to the localized photodimerization, the number of An-IL that originally interacted with IL in the exposed region became decreased, and therefore the IL droplets become freely move in the system. As the heating time increased, the free IL droplets began to collide and coalescence to grow and finally secreted out of the surface of primary patterns. Regarding the non-exposed region, the interaction between IL and An-IL was unchanged and thus there were no IL droplets separation occurred. In addition, when the molar ratios of IL reached too high, An-PIL tend to form a highly solvated network structure in IL bulk, and both An-IL and BA segments were solvated by a large amount of IL, thus the iontronic host became highly soft and the free IL droplets more likely to move into IL bulk instead of secreting out.

## 2.3 Ionic electrical performance of IL droplets @primary patterns

Thanks to the flexibility and adaptability of the photodimerization crosslinking and heat treatment process, a series of IL droplets @patterns (where the molar ratio of An-PIL to IL in the iontronic host is 1:2) can be readily fabricated, as shown in Fig. 3A. Due to the localized secretion of IL and thus resulting in the different content of mobile anions and cations within the unexposed and exposure regions, various micropatterns with distinct ionic conductivity can be fabricated by using corresponding photomasks and

simultaneous controlling the subsequent heating time. To illustrate the unique iontronic features of IL droplets @primary patterns, the conductive AFM (C-AFM) measurement (Fig. 3B) was used to test the point contact I-V curves for different regions corresponding to a representative doughnut-like primary patterns. As shown in Figs. 3C-D, the positive and negative currents exhibit obvious nonlinear characteristics for both unexposed and exposure regions, indicating that the Schottky contact was formed between the Pt-coated tips and primary patterns. In addition, the positive bias current was significantly higher than that of the negative bias current for the unexposed region (i.e. the pristine iontronic host) by comparing the current changes in Fig. 3C. According to the ionic conduction mechanism<sup>36, 37, 38</sup>, the transport of ions among ionic polymeric networks is driven by the ion jumps over an energy barrier among coordinative polar groups on the polymer matrix. As for the iontronic host in this work, the  $T_g$  decreased with the higher addition of IL (Figure S6) and thus the free ions can easily transport among An-PIL. Moreover, since the anions (free [TFSI]<sup>-</sup> groups) were bound by the polyimidazolium cation of An-PIL via the electrostatic force. Thus, the cations (free imidazolium groups) were the main mobile ions and result in a rectification effect under positive and negative bias. Besides, due to the cross-linked polymeric ionic network generated in exposure regions, free ions were hard to transport, and thus the current for exposure regions was smaller than that of the unexposed region, as shown in Fig. 3C and Fig. 3D. Further results on the current curves showed that the tunnel current for both unexposed and exposure regions were associated with IL content. The largest tunnel current appeared at the molar ratio of An-PIL to IL of 1:2, which can be explained by the intrinsic phase structure change of iontronic host. When less IL was added to An-PIL (i.e. the molar ratios of An-PIL to IL were 1:1), the rigid polymeric ionic network will hinder the ionic conduction and fewer free ions could transport above the  $T_g$  of iontronic host at the same bias voltage, resulting in smaller tunnel current. In comparison, when much IL was added into An-PIL (i.e. the molar ratios of An-PIL to IL were 1:3), the iontronic host became softer and a substantial amount of IL accumulated at the bottom layer of iontronic host due to the higher density of IL than that of An-PIL. Therefore, the free ions content at the interface between the pattern and the tips was lower and resulted in a smaller tunnel current. Thus, the ionic conductivity of the patterns can be regulated by controlling the molar ratio of An-PIL to IL in iontronic hosts.

Besides, the interfacial capacitance of iontronic hosts before and after micropatterning has been investigated. Based on the polarization characteristics of An-PIL and a large number of free ions in iontronic host, the electric double layer (EDL) capacitance can readily be generated between the accumulated positive and negative charges on the two opposite electrodes and the corresponding cations and anions, as shown in Fig. 3E. The resultant interfacial capacitance against excitation frequency and molar ratios has been summarized in Fig. 2F-G. As expected, the EDL capacitance was highly frequency-dependent and the unit-area capacitance gradually decreased with a rising frequency. The capacitance-frequency curve of the exposure samples (i.e. the IL @primary patterns) exhibits a similar trend to that of unexposed samples (i.e. the pristine iontronic host) during the same frequency range (20 Hz to 2 MHz). In particular, the unit-area capacitances of pristine iontronic hosts were  $1.69 \mu\text{F cm}^{-2}$ ,  $1.35 \mu\text{F cm}^{-2}$ , and  $0.67 \mu\text{F cm}^{-2}$  (20 Hz) corresponding to the molar ratios of An-PIL to IL were 1:2, 1:3, and 1:1, respectively, as shown in Fig. 3F. However, regarding the IL @primary patterns containing

different molar ratios of An-PIL to IL, the unit-area capacitances declined to  $0.68 \mu\text{F cm}^{-2}$ ,  $0.025 \mu\text{F cm}^{-2}$ , and  $0.002 \mu\text{F cm}^{-2}$ , respectively, as shown in Fig. 3G. Thus, higher molar ratios of IL in iontronic hosts will result in an appreciable decline in the interfacial capacitance at the same excitation frequency. Finally, with the requirements of higher capacitance and highly patterned surface, the IL @primary patterns comprise of molar ratios of An-PIL to IL was 1:2 as the optimal samples for the following secondary wrinkles construction.

## 2.4 Construction of secondary iontronic wrinkles

Owing to the good solubility of 3,4-ethylenedioxythiophene (EDOT) in [EMIm][TFSI] (i.e. the IL in this work), the IL @primary patterns can be developed to be a microreactor vessel for the synthesis of PEDOT, as shown in Figure S7. The resultant PEDOT on primary patterns were shown in Fig. 4A-C. Among these, IL droplets firstly absorbed EDOT vapor and then processed with oxidative polymerization in the presence of iodine vapor. Thereafter, the IL-doped PEDOT was finally synthesized and secondary wrinkles appeared simultaneously, as shown in Fig. 4B. Notably, when a lower or higher molar ratio of IL was added in primary patterns (i.e., corresponding to the molar ratios of An-PIL to IL in Fig. 4a and Fig. 4c were 1:1 and 1:5, respectively), the IL droplets will not secrete onto primary patterns according to the above results in Fig. 2, and thus the EDOT vapor can only be absorbed on the surface of primary patterns, and ultimately lead to no PEDOT generated in Fig. 4A as well as the randomly distributed grainy PEDOT appeared in Fig. 4C. Subsequently, microscopic attenuated total reflection infrared spectroscopy (ATR) was used to characterize the surface components variation of IL droplets @primary patterns after vapor oxidative polymerization of PEDOT (Fig. 4D). The characteristic peaks at  $1726 \text{ cm}^{-1}$  are assigned to ester groups of BA segment on An-PIL, and bands located at  $1340$  and  $1184 \text{ cm}^{-1}$  are attributed to asymmetric and symmetric stretching vibrations of  $\text{O}=\text{S}=\text{O}$  group of  $\text{TFSI}^-$ , respectively. Besides, the peak at  $1049 \text{ cm}^{-1}$  was the characteristic stretching vibration of S-N-S in TFSI anions<sup>39,40</sup>. Since the chemical structure of IL was similar to that of An-PIL, therefore no significant changes in characteristic peaks after photodimerization and heating of iontronic host, as shown in the spectra of IL @primary patterns. Moreover, new peaks at  $1534$ ,  $1397$ , and  $1250 \text{ cm}^{-1}$  were attributed to the C=C and C-C stretching vibrations of the quinoid structure of the thiophene ring, respectively. Besides, the band at about  $1250 \text{ cm}^{-1}$  was due to the C-O-C bond stretching in the ethylene dioxy (alkylenedioxy) group. The series of bands agreed with the literatures<sup>41,42</sup>, suggesting the formation of IL-doped PEDOT.

To understand the buckling mechanism for secondary wrinkles, we tracked the morphological changes of the primary patterns, as shown in Fig. 4E. As EDOT evaporated and adsorbed into IL droplets at  $120^\circ\text{C}$ , secondary wrinkles generated onto the unexposed regions of primary patterns after cooling. Meanwhile, the diameter of IL droplets became larger and the primary patterns turned to be swollen after absorbing EDOT. After further processing in the atmosphere of Iodine vapor, IL-doped PEDOT appeared on the surface of primary patterns, while pure PEDOT (i.e., non-IL doping PEDOT) was generated on the secondary wrinkles. To clarify the reasons for the production of secondary wrinkles, a modified bilayer system that incorporates the stiff primary patterns (surface layer) and the soft iontronic host (substrate)

was proposed in Fig. 4F according to our previous work<sup>28, 43</sup>. Since the internal polymeric matrix of the primary pattern was crosslinked and showed a higher modulus, the pristine iontronic host (substrate layer) has a larger expansion coefficient relative to that of the primary patterns. The thermal expansion of the unexposed area was bound by the primary patterns during heating treatment, resulting in the accumulation of internal stress at the interface between primary patterns and unexposed regions. Moreover, EDOT vapor is more inclined to be adsorbed by IL droplets, and also a small amount of EDOT vapor will be adsorbed on unexposed regions. Therefore, the internal stress accumulated in stiff primary patterns will release during cooling and thus squeezing the softer unexposed regions to produce the typical wrinkle pattern. At the same time, IL-doped and raw PEDOT were produced on the surfaces of primary patterns and secondary wrinkles, respectively due to the oxidation of iodine vapor.

In addition, by controlling the polymerization time of PEDOT, secondary wrinkles with different amplitudes can be regulated as shown in Fig. 4G. This process can also be illustrated by a typical bilayer model incorporated with the secondary wrinkles acting as the softer substrate layer and the rigid PEDOT serving as the stiff surface layer. When the vapor polymerization time was short than 2 h, the peak of the secondary wrinkles was firstly exposed to iodine vapor and thus PEDOT was generated onto the peaks, which resulted in the interlayer stress increasing continuously, and that is the wavelength and amplitude also increasing<sup>44</sup>. When the reaction time was longer than 4 h, PEDOT will also produce in the trough region of secondary wrinkles, which causes an increase in the height of the trough, and thus the height difference between the peak and the trough decreases, and that is the wavelength and amplitude also decrease. Moreover, when the reaction time was furtherly increased to 20 h, the PEDOT layers covered on both the peaks and troughs were continuously thickened, and the wavelength and amplitude increased simultaneously. Notably, due to the excessive local stress relief, when the gas phase polymerization time was higher than 12 h, the resulting PEDOT gradually formed films and cracked, as shown in Fig. 4G. Therefore, considering the structural integrity and electrical conductivity of PEDOT, the HAMI prepared at 12 h will be used for the following study.

## 2.5 Asymmetric Ionic electrical performance of HAIM

Figure 5A-B showed the morphology of the as-prepared HAIM. Owing to the boundary constraints of the primary patterns, long-range wrinkle patterns in the area I parallel to the boundary were produced on the surface of the unexposed region. However, labyrinth-like wrinkle patterns in area II were generated in the unexposed regions. The distinct wrinkling patterns were caused by the different boundary constraints condition<sup>31</sup>. The LSCM images in Fig. 5C showed the amplitude of labyrinth wrinkles in area was lower than that of the parallel wrinkles in area , which was consistent with the results in Fig. 4G-H. In addition, Fig. 5D exhibited spherical PEDOT bonded to each other in area while flake PEDOT distributed discretely in area . In terms of area I (i.e., IL droplets @primary patterns), the polymerization of EDOT was carried out in IL droplets. Moreover, since the strong polarity of IL and the electrostatic interaction between IL with the PEDOT main chain, it is difficult to form a linear arrangement and stacking for the resultant spherical IL-doped PEDOT<sup>45</sup>. However, as for the chemical environment of area II, the EDOT was

polymerized on the unexposed regions and without IL droplets doping, therefore the structure of the as-prepared PEDOT tended to be complete and flaky. To further illustrate the asymmetric shape of the resultant PEDOT, Energy Dispersive Spectroscopy (EDS) tests for PEDOT on both primary patterns and secondary wrinkles were conducted in Fig. 5E and Figure S8. Comparing with the change of surface atomic weight percentage for different regions, it can be found that the nitrogen content in PEDOT @secondary patterns (area ) was close to 0% while in PEDOT @primary patterns (area I) was 3.85%. Moreover, since the EODT itself does not contain nitrogen and thus the nitrogen in polymeric EDOT can only from the contribution of IL doping. In addition, since iodide ions were the counterion for pure PEDOT in area II while [TFSI]<sup>-</sup> groups may also become the counterion of IL-doped PEDOT in area I, thus the content of iodide in area II (22.54%) was obviously higher than that of area I (11.53%). In sum, the above results showed that the asymmetric PEDOT can be synthesized by developing different vapor polymerization environments on primary patterns.

The ionic electrical performance of as-prepared HAIM was performed through homemade encapsulation devices in Fig. 5F. The interface capacitance (Fig. 5G) was obtained from connecting point B and point C to a digital multi-meter. Since the IL secretion and thus the mobile ions reduced in primary patterns, the capacitance decreased from 1.69  $\mu\text{F cm}^{-2}$  for pristine iontronic host to that of 0.68  $\mu\text{F cm}^{-2}$  for IL @primary patterns, and to that of 0.007  $\mu\text{F cm}^{-2}$  for HAIM at the same frequency of 20 Hz. In addition, the surface resistivity (Fig. 5H) was conducted by connecting point A and point B or C to a digital multi-meter. With the production of conductive PEDOT on the surface of iontronic host, its surface resistivity decreased from the original of 3.7  $\text{M}\Omega\cdot\text{cm}^{-1}$  to 2.33  $\text{M}\Omega\cdot\text{cm}^{-1}$  for that of the PEDOT @exposure regions (area ) and to 0.6  $\text{M}\Omega\cdot\text{cm}^{-1}$  for that of the PEDOT @unexposed region (area ). Thereafter, the asymmetric conductive micropatterns provide sufficient conditions for the realization of piezoionic effect and resulted in a potential gradient between area and area , as shown in Fig. 5I. Generally, the piezoionic effect is a result of Donnan-like depolarization due to an inhomogeneous ionic distribution<sup>33</sup>. In terms of the HAIM, the IL-doped PEDOT initially at equilibrium has a uniform distribution of mobile species such that the electrochemical potential experienced by all species is equal and the free energy of the system is minimal. When a mechanical perturbation causes HAIM to non-homogeneously deform, the ionic species will experience a differential pressure locally and displace to result in the chemical potential change. At this depolarized state, the change in chemical potential directly corresponded to the change in electrical potential measured. This electrical potential change,  $\Delta E$ , can be estimated as in Eq. 1

$$\Delta E = \frac{RT}{ZF} \ln \left( \frac{[i]_x}{[i]_{x+\Delta x}} \right)$$

1

Where  $R$  is the gas constant,  $T$  is the temperature,  $Z$  is the valence charge of the ion,  $F$  is Faraday's constant;  $[i]$  represents the concentration of the  $i$ th species and the subscripts represent two locations separated by a distance  $\Delta x$  within the sample. The detailed mathematical derivation was shown in the

Figure S9. Clearly, the potential gradient of HAIM is determined by the value of  $[i]_x/[i]_{x+\Delta x}$ . Higher content of ions in pristine iontronic host can easily displace to achieve a significant ions gradient, providing the larger potential gradient of -64.5 mV. However, since the diffusion and drifting of free ions in pristine iontronic host, the resultant potential gradient decreased to -1 mV after 1 min interval. Moreover, due to the photodimerization cross-linking and IL secretion among primary patterns, the IL content decreased and the ion gradient reduced, resulting in the potential gradient between the primary patterns and the unexposed region decreased to -21.6 mV and declined to -5 mV after 1 min. In particular, the potential gradient between IL-doped PEDOT on primary patterns and raw PEDOT on secondary wrinkles was stably maintained at -35.7 mV due to the stable ions gradient difference as mentioned in Fig. 1F. Thus, the vapor polymerization of asymmetric PEDOT plays a vital role in the potentiometric gradient.

## 2.6 Regulation of the potentiometric gradient for HAIM

With the above results in mind, we further demonstrated the controlling of vapor polymerization time as the key to potentiometric gradient regulation. To facilitate integrate HAIM to an external circuit, an evenly spaced stripes-like HAIM was prepared and which enabled the negative and positive to be arranged in a tandem array (Fig. 6A). The LSCM images of the as-prepared HAIM (Fig. 6B) showed a similar morphology corresponding to the above results in Fig. 5B. The micromorphology of raw PEDOT on secondary wrinkles and the IL-doped PEDOT on primary patterns were shown in Fig. 6C-F. As the polymerization times increased, spherical IL-doped PEDOT gradually joined to form a conductive film onto the primary patterns in Fig. 6F. Meanwhile, the interface capacitance between HAIM and Au-coated interdigital electrodes decreased with the polymerization time increased, as shown in Fig. 6F. Notably, the largest interfacial capacitance of HAIM appeared at the polymerization time of 12 h and which decreased slowly with frequency change. The higher interfacial capacitance indicates that more mobile ions can be polarized in IL-doped PEDOT under an external electric field and which was consistent with the surface resistivity variations in Figure H. In terms of the different surface resistivity for HAIM, both  $[I]^-$  and  $[TFSI]^-$  groups can become the counterion anion of PEDOT during the polymerization processes. Regarding to IL-doped PEDOT on primary patterns, the IL would have electrostatic interactions with the main chain of PEDOT and iodide ions, resulting in a reduction in the structural integrity of the as-prepared PEDOT and also a decrease in the conjugation length of  $\pi$  bonds<sup>46</sup>. Therefore, the surface resistivity for IL-doped PEDOT was higher than that of raw PEDOT. In addition, the surface resistivity for raw PEDOT on unexposed regions were obviously lower than that of point I (pristine iontronic host), point II (IL droplets @primary patterns), and point III (the IL @primary patterns after absorbing EDOT). Specifically, the lowest surface resistivity for raw PEDOT on secondary wrinkles dropped to  $0.58 \text{ M}\Omega\cdot\text{cm}^{-1}$  when the reaction was carried out for 12 h. Meanwhile, the surface resistivity for IL-doped PEDOT on primary patterns decreased slowly with polymerization time, and the lowest value was  $2.33 \text{ M}\Omega\cdot\text{cm}^{-1}$ . According to these results, we proposed that the surface resistivity was initially dominated by IL content and the continuous production of PEDOT which enabled HAIM to exhibit higher conductivity. Furthermore, when the reaction time reaches 20 h, the excess iodine vapor is adsorbed on the surface of HAIM, resulting in lower ionic conduction and higher surface resistivity for HAIM.

Because IL-doped PEDOT was filled with free mobile ions, and the main chain regularity of IL-doped PEDOT was low, therefore the ions in the original equilibrium state can readily be redistributed and thus ions gradient will generate under the action of external force. In addition, the cations in IL-doped PEDOT are more easily migrated relative to the anions under the action of external force, therefore, excess anions will accumulate at the surface, resulting in a negative potential, as shown in Fig. 6l. However, IL-PEDOT will gradually form a film and become rigid with the increase of polymerization time, resulting in the reduction of ion migration and gradient under the external force, which also reduces the open circuit potential gradient between the asymmetric regions. These results indicate that the HAMI could serve as a force-induced electrical generator, implying its potential broad applications in iontronic power generators.

### 3 Discussion

In conclusion, we have demonstrated a down-top, interlocked patterning strategy for the scalable fabrication of hierarchical and asymmetrical iontronic micropatterns through the combination of photodimerization and vapor oxidative polymerization. Locally photodimerization crosslinking and subsequent heating produce an IL droplet covered primary patterns-based microreactor and pristine iontronic host-based secondary wrinkles. The resultant IL-doped PEDOT and raw PEDOT on HAIM can respond to the external compression and readily generate potential gradients based on piezoionic effect. The morphology and electrical performance of HAIM can be controlled by the constrained boundary conditions and the polymerization time. It is believed that such an exceptional fabrication method, which combines the advantages of top-down and bottom-up approaches, can provide a brand-new choice for on-demand surface patterning of iontronic materials. We envision that the HAIM will open up an opportunity for a range of applications in pressure sensors, force-induced potential generators, and electrochemical deposition.

## 4 Experiment Section

### 4.1 Fabrication of IL @primary patterns

In this work, anthracene-functionalized ionic liquid copolymer (denote as An-PIL) was plasticized by 1-ethyl-3-methylimidazolium bistrifluoromethylsulfonimide lithium (denoted as IL). Firstly, a 5 wt.% An-PIL solution was prepared in DMF, and then IL was added into the solutions according to the molar ratios of the An-IL segment to IL of 1:0, 1:0.5, 1:1, 1:2, 1:3, 1:5 and 1:10, respectively. Thereafter, the homogeneous iontronic hosts were obtained from twice filtration with 0.22  $\mu\text{m}$  Teflon syringe-driven filter. Subsequently, drop coating of the above mixing solution on a glass plate or PET film and then an iontronic film with thickness of a 45  $\mu\text{m}$  was obtained after drying at 90  $^{\circ}\text{C}$  for 20 min. Finally, upon the irradiation of ultraviolet (UV) light for 15 min (LED UV lamp, 365 nm, 15  $\text{mW}/\text{cm}^2$ ), the desired primary patterns can be obtained by using different photomasks. Thereafter, the resulting primary patterns were heated at 85 $^{\circ}\text{C}$  for different times to secrete IL droplets from the surface of the primary patterns (denoted as IL @primary patterns).

## 4.2 Preparation of Secondary wrinkles

A homemade hotplate setup was used for EDOT diffusion into IL droplets @primary patterns. Firstly, IL droplets @primary patterns were stuck to a glass petri dish and then placed it upside down to cover 5  $\mu$ L EDOT on a hotplate. After heating at 120 °C for 20 min, IL droplets @primary patterns with a weight increment of 2.9 mg were removed and placed in a crimp cap vial together with iodine (59.7 mg). The crimp cap vial was heated to 70 °C for 2 h, 4 h, 8 h, 12 h, and 20 h in a synthesis oven, respectively, to the realization of PEDOT-coated primary patterns and secondary wrinkles.

## Declarations

### Acknowledgments

The authors thank National Nature Science Foundation of China (52025032 and 52103144) for their financial support.

### Author Contributions

X. J. and J. Y. conceived the research and analyzed the results and data; Z. W. carried out the material synthesis and characterization; T. L. and J. L. took part in some work of material synthesis. Y. C and X. M tested the application properties. All authors contributed to the manuscript.

### Competing interests

The authors declare no competing interests.

### Additional information

Supplementary information

Data supporting the findings of this study are available within the paper and its supplementary information files. All other relevant data that support the findings of this study are available from the corresponding author upon request.

## References

1. Hou H, Yin J, Jiang X. Smart patterned surface with dynamic wrinkles. *Accounts of chemical research* **52**, 1025–1035 (2019).
2. Wu P, Wang J, Jiang L. Bio-inspired photonic crystal patterns. *Materials Horizons* **7**, 338–365 (2020).
3. Dai H, Dong Z, Jiang L. Directional liquid dynamics of interfaces with superwettability. *Science Advances* **6**, eabb5528 (2020).
4. Schroeder TB, *et al.* An electric-eel-inspired soft power source from stacked hydrogels. *Nature* **552**, 214–218 (2017).

5. Kobayashi T, Menon AK. Transbilayer lipid asymmetry. *Current Biology* **28**, R386-R391 (2018).
6. Cheng X, Smith JC. Biological membrane organization and cellular signaling. *Chemical reviews* **119**, 5849–5880 (2019).
7. He C, Sun S, Wu P. Intrinsically stretchable sheath-core ionic sensory fibers with well-regulated conformal and reprogrammable buckling. *Materials Horizons* **8**, 2088–2096 (2021).
8. Jin ML, *et al.* An ultrasensitive, visco-poroelastic artificial mechanotransducer skin Inspired by piezo2 protein in mammalian merkel cells. *Advanced Materials* **29**, 1605973 (2017).
9. Latorre R, HALL JE. Dipole potential measurements in asymmetric membranes. *Nature* **264**, 361–363 (1976).
10. Wang H, *et al.* Bilayer of polyelectrolyte films for spontaneous power generation in air up to an integrated 1,000 V output. *Nature Nanotechnology* **16**, 811–819 (2021).
11. Ren Y, *et al.* Electric-Field-Induced Gradient Ionogels for Highly Sensitive, Broad-Range-Response, and Freeze/Heat-Resistant Ionic Fingers. *Advanced Materials* **33**, 2008486 (2021).
12. Lee JI, *et al.* Visco-Poroelastic Electrochemiluminescence Skin with Piezo-Ionic Effect. *Advanced Materials* **33**, 2100321 (2021).
13. Kim HJ, Chen B, Suo Z, Hayward RC. Ionoelastomer junctions between polymer networks of fixed anions and cations. *Science* **367**, 773–776 (2020).
14. Qiu Z, *et al.* Ionic skin with biomimetic dielectric layer templated from calathea zebrine leaf. *Advanced Functional Materials* **28**, 1802343 (2018).
15. Chang Y, *et al.* First decade of interfacial iontronic sensing: from droplet sensors to artificial skins. *Advanced Materials* **33**, 2003464 (2021).
16. Laucirica G, Albesa AG, Toimil-Molares ME, Trautmann C, Marmisollé WA, Azzaroni O. Shape matters: Enhanced osmotic energy harvesting in bullet-shaped nanochannels. *Nano Energy* **71**, 104612 (2020).
17. Li M, Wang C, Liu Z, Song Y, Li D. Ionic Diode Based on an Asymmetric-Shaped Carbon Black Nanoparticle Membrane. *Advanced Functional Materials* **31**, 2104341 (2021).
18. Bai L, *et al.* Bio-inspired Visual Multi-sensing Interactive Ionic Skin with Asymmetrical Adhesive, Antibacterial and Self-powered Functions. *Chemical Engineering Journal*, 135596 (2022).
19. Biswas A, Bayer IS, Biris AS, Wang T, Dervishi E, Faupel F. Advances in top-down and bottom-up surface nanofabrication: Techniques, applications & future prospects. *Advances in colloid and interface science* **170**, 2–27 (2012).
20. Harwell J, Burch J, Fikouras A, Gather MC, Di Falco A, Samuel ID. Patterning multicolor hybrid perovskite films via top-down lithography. *ACS nano* **13**, 3823–3829 (2019).
21. Bae WG, Kim HN, Kim D, Park SH, Jeong HE, Suh KY. 25th anniversary article: scalable multiscale patterned structures inspired by nature: the role of hierarchy. *Advanced Materials* **26**, 675–700 (2014).

22. Wu S, *et al.* Hydrogel patterning with catechol enables networked electron flow. *Advanced Functional Materials* **31**, 2007709 (2021).
23. Bowden N, Brittain S, Evans AG, Hutchinson JW, Whitesides GM. Spontaneous formation of ordered structures in thin films of metals supported on an elastomeric polymer. *nature* **393**, 146–149 (1998).
24. Cera L, Schalley CA. Under diffusion control: from structuring matter to directional motion. *Advanced Materials* **30**, 1707029 (2018).
25. Liu M, Wang S, Jiang L. Nature-inspired superwettability systems. *Nature Reviews Materials* **2**, 1–17 (2017).
26. Efimenko K, Rackaitis M, Manias E, Vaziri A, Mahadevan L, Genzer J. Nested self-similar wrinkling patterns in skins. *Nature materials* **4**, 293–297 (2005).
27. Yang S, Khare K, Lin PC. Harnessing surface wrinkle patterns in soft matter. *Advanced Functional Materials* **20**, 2550–2564 (2010).
28. Hou H, *et al.* Reversible surface patterning by dynamic crosslink gradients: controlling buckling in 2D. *Advanced Materials* **30**, 1803463 (2018).
29. Saruwatari A, Tamate R, Kokubo H, Watanabe M. Photohealable ion gels based on the reversible dimerisation of anthracene. *Chemical communications* **54**, 13371–13374 (2018).
30. Tomé LC, Porcarelli L, Bara JE, Forsyth M, Mecerreyes D. Emerging iongel materials towards applications in energy and bioelectronics. *Materials Horizons* **8**, 3239–3265 (2021).
31. Zhou L, Hu K, Zhang W, Meng G, Yin J, Jiang X. Regulating surface wrinkles using light. *National science review* **7**, 1247–1257 (2020).
32. Ren Y, *et al.* Ionic liquid-based click-ionogels. *Science advances* **5**, eaax0648 (2019).
33. Mirza S, *et al.* Transparent and conformal piezoionic touch sensor. In: *Electroactive Polymer Actuators and Devices (EAPAD) 2015*. International Society for Optics and Photonics (2015).
34. Li M, *et al.* Gel-Electrolyte-Coated Carbon Nanotube Yarns for Self-Powered and Knittable Piezoionic Sensors. *ACS Applied Electronic Materials* **3**, 944–954 (2021).
35. Dobashi Y, *et al.* Piezoionic mechanoreceptors: Force-induced current generation in hydrogels. *Science* **376**, 502–507 (2022).
36. Wu F, *et al.* Solid state ionics-selected topics and new directions. *Progress in Materials Science*, 100921 (2022).
37. Griffin PJ, *et al.* Ion transport in cyclopropenium-based polymerized ionic liquids. *Macromolecules* **51**, 1681–1687 (2018).
38. Bocharova V, Sokolov AP. Perspectives for polymer electrolytes: a view from fundamentals of ionic conductivity. *Macromolecules* **53**, 4141–4157 (2020).
39. Wang Z, Si Y, Zhao C, Yu D, Wang W, Sun G. Flexible and washable poly (ionic liquid) nanofibrous membrane with moisture proof pressure sensing for real-life wearable electronics. *ACS applied materials & interfaces* **11**, 27200–27209 (2019).

40. Wang Z, Wang W, Sun G, Yu D. Designed ionic microchannels for ultrasensitive detection and efficient removal of formaldehyde in an aqueous solution. *ACS Applied Materials & Interfaces* **12**, 1806–1816 (2019).
41. Zhang J, Zhao X. Conducting polymers directly coated on reduced graphene oxide sheets as high-performance supercapacitor electrodes. *The Journal of Physical Chemistry C* **116**, 5420–5426 (2012).
42. Le Ouay B, Boudot M, Kitao T, Yanagida T, Kitagawa S, Uemura T. Nanostructuring of PEDOT in porous coordination polymers for tunable porosity and conductivity. *Journal of the American Chemical Society* **138**, 10088–10091 (2016).
43. Li F, Hou H, Yin J, Jiang X. Near-infrared light-responsive dynamic wrinkle patterns. *Science Advances* **4**, eaar5762 (2018).
44. Gao X, *et al.* Photo-Polymerization Induced Hierarchical Pattern via Self-Wrinkling. *Advanced Functional Materials* **31**, 2106754 (2021).
45. Kee S, *et al.* Controlling molecular ordering in aqueous conducting polymers using ionic liquids. *Advanced Materials* **28**, 8625–8631 (2016).
46. Elschner A, Kirchmeyer S, Lovenich W, Merker U, Reuter K. *PEDOT: principles and applications of an intrinsically conductive polymer*. CRC press (2010).

## Figures

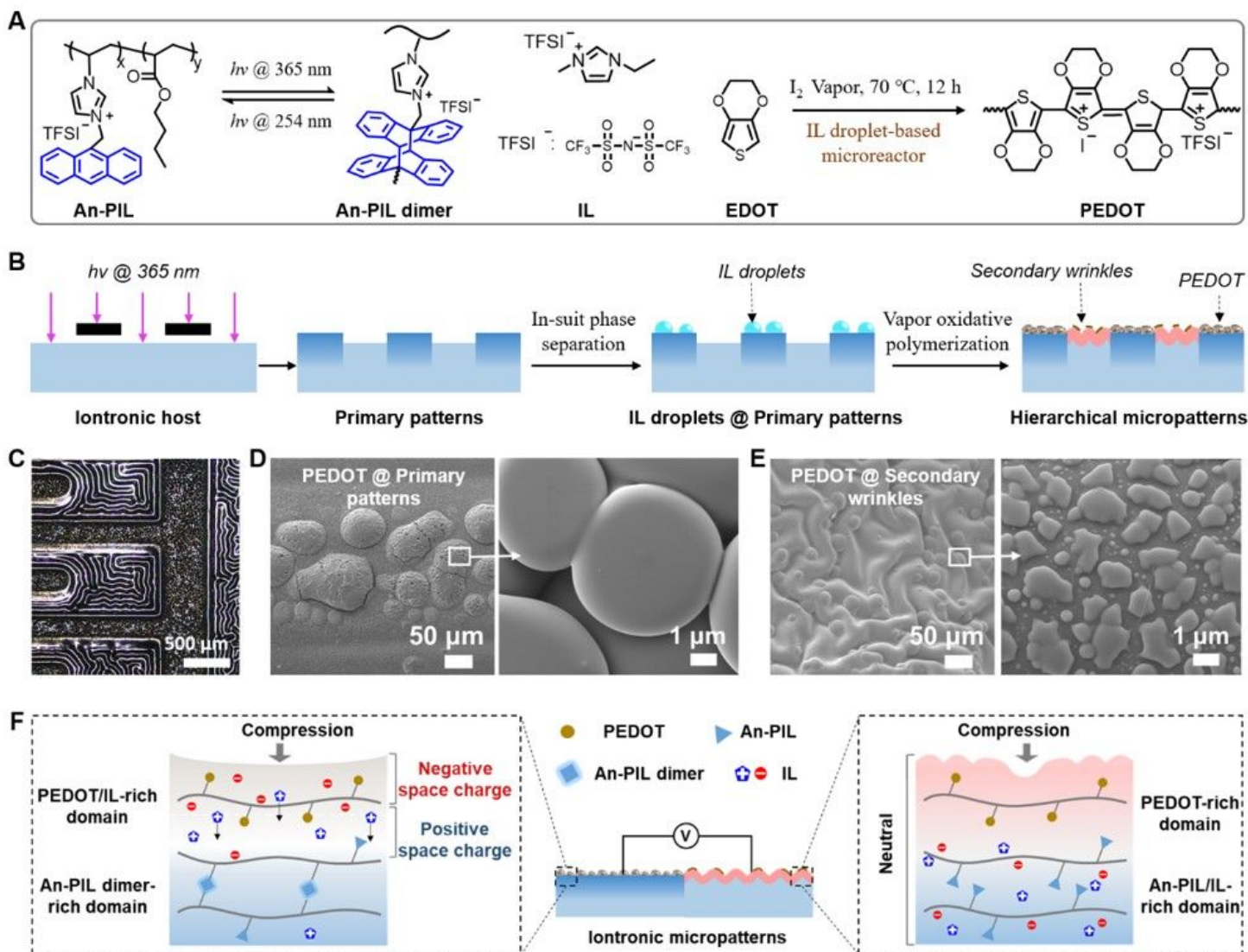


**Figure 1**

Design, structure, and piezoionic effect of HAIM. (A) Chemical structure of An-PIL, An-PIL dimer, IL, and PEDOT. (B) The fabrication process for HAIM through localized photodimerization and vapor oxidative polymerization. (C) Microscope images of a representative HAIM sample. FSEM images of PEDOT on (D) primary patterns and (E) secondary wrinkles, respectively. (F) Proposed mechanism for the potential gradient between IL-doped PEDOT @primary and pure PEDOT @secondary wrinkles.

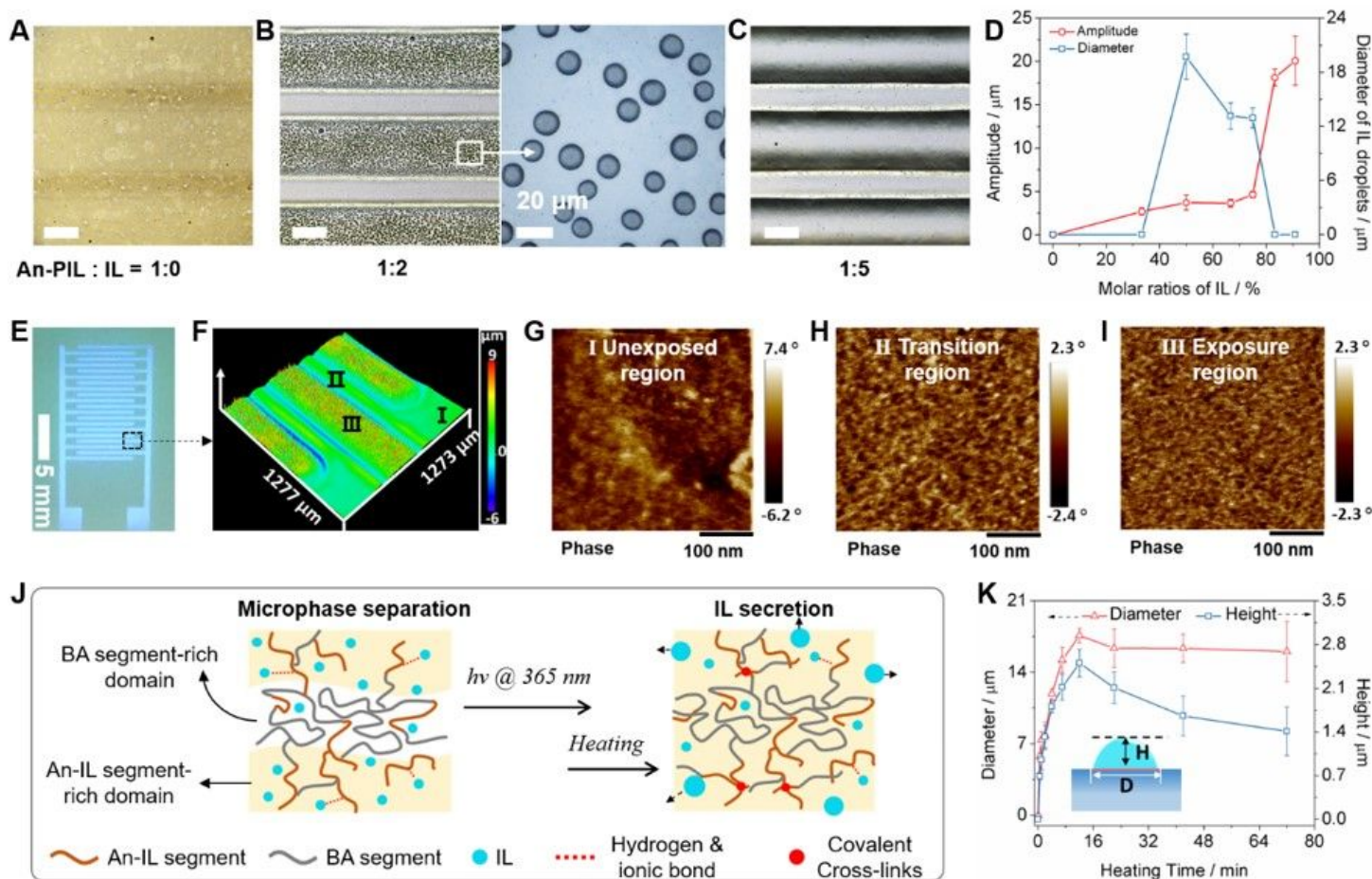


**Figure 2**

Photodimerization and *in-suit* phase separation of the iontronic host. (A)-(C) are microscopy images of iontronic hosts after photodimerization crosslinking and heating, scale bar: 200  $\mu\text{m}$ . (D) The amplitude variation of the primary patterns and the diameter change of the IL droplets versus the molar ratios of IL. (E) fluorescence image and (F) the corresponding LSCM image of the as-prepared primary patterns. AFM phase images of (G) unexposed region, (H) transition region, and (I) exposure region corresponding to (F). (J) The proposed phase separation mechanisms for iontronic hosts after photodimerization crosslinking and heating. (K) The diameter and height change of the IL droplets versus the heating time.

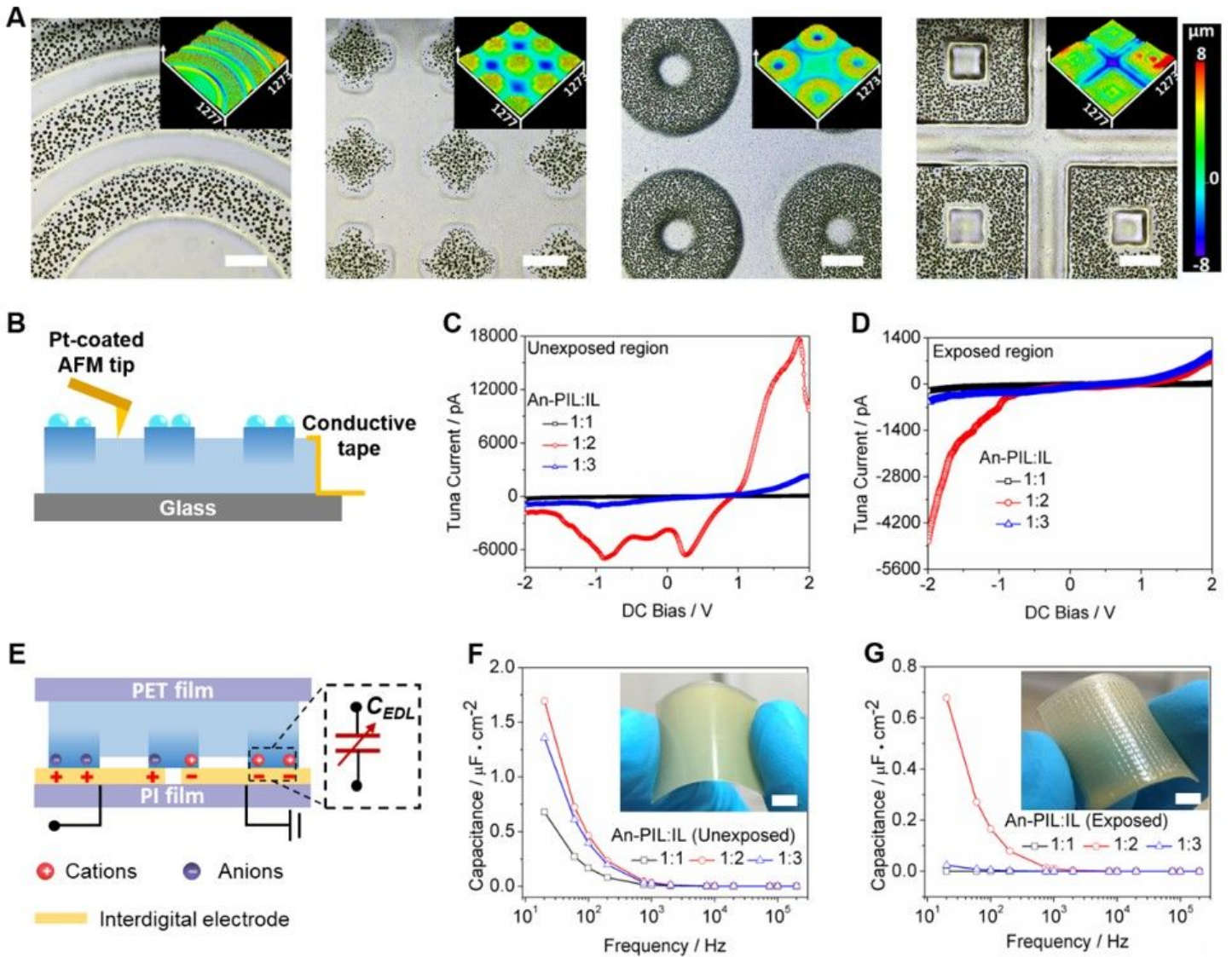


**Figure 3**

Localized regulation of the ionic electrical performance of primary patterns. (A) Microscopy images show IL droplets @ primary patterns, scale bar: 200  $\mu\text{m}$ . (B) Schematic diagram of the conductivity AFM measurement (C-AFM) for IL droplets @primary patterns. Averaged point contact I-V curve obtained after averaging I-V responses from 15 different spots shown in (C) unexposed regions (i.e., pristine iontronic host) and (D) exposure regions (i.e., IL droplets @primary patterns) with different molar ratios of An-PIL to IL. (E) The schematic diagram for the EDL capacitance between interdigital electrodes and IL droplets @primary patterns. Interfacial capacitance changes at different frequencies for (F) unexposed regions (i.e., pristine iontronic host) and (G) exposure regions (i.e., IL droplets @primary patterns) with different molar ratios of An-PIL to IL, the insert were the optical images of pristine iontronic host and micropatterned iontronic host, respectively, scale bar: 1 cm.

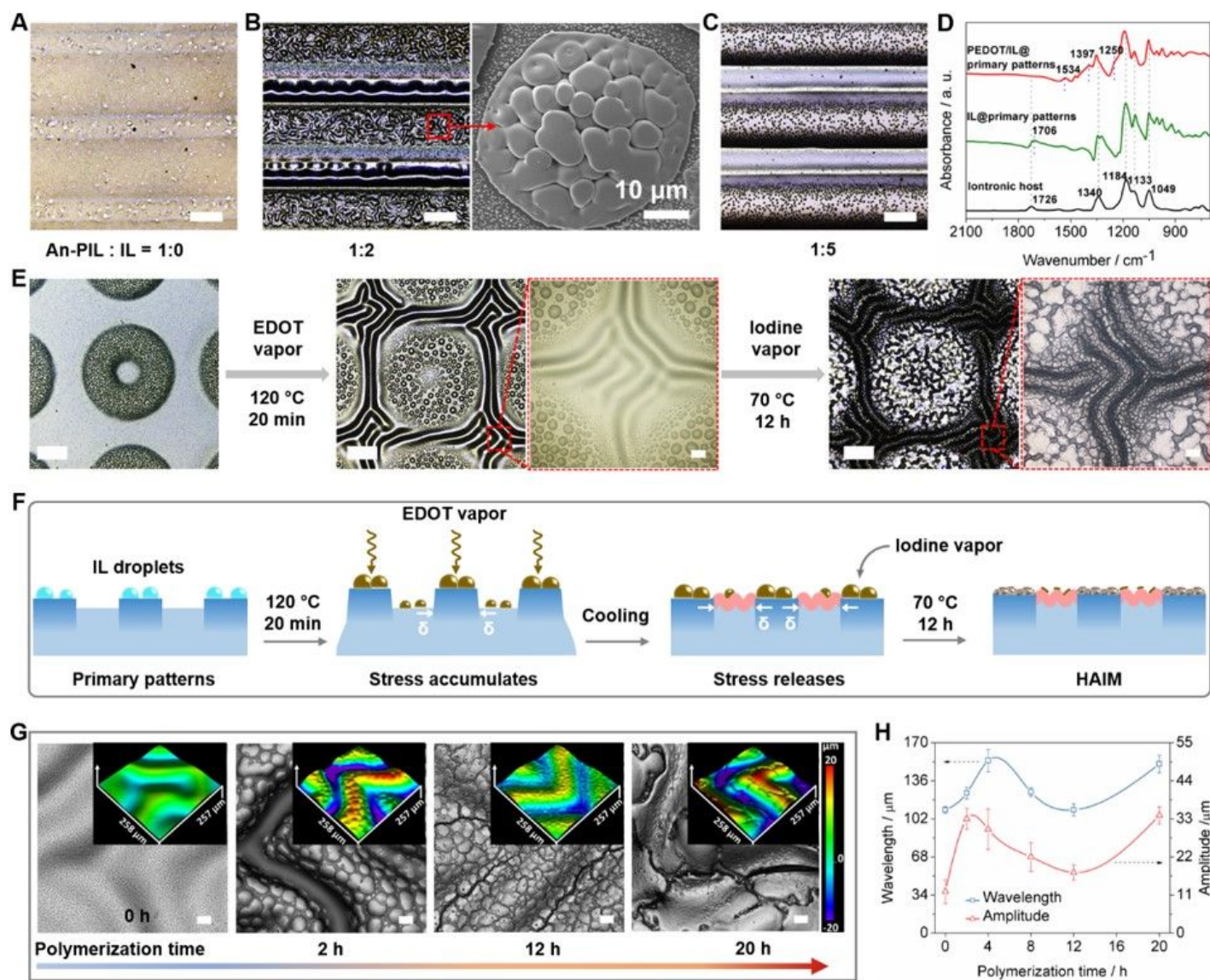


**Figure 4**

Fabrication, characterization, and mechanisms of secondary wrinkles. (A-C) optical microscope images of synthesized PEDOT on the surface of primary patterns containing different molar ratios of IL, scale bar:200  $\mu\text{m}$ . (D) FTIR spectra for iontronic host, IL droplets @primary patterns, and resultant HAIM. (E) Optical microscope images of the morphology variation for the fabrication of secondary wrinkles, scale bar:200  $\mu\text{m}$ , scale bar of enlarged images: 20  $\mu\text{m}$ . (F) Schematic demonstration of the fabrication of secondary wrinkles. (G) The optical microscope images of secondary wrinkles against polymerization times, scale bar: 50  $\mu\text{m}$ , the insert was the corresponding LSCM images. (H) The wavelength and amplitude change of secondary wrinkles versus polymerization time.

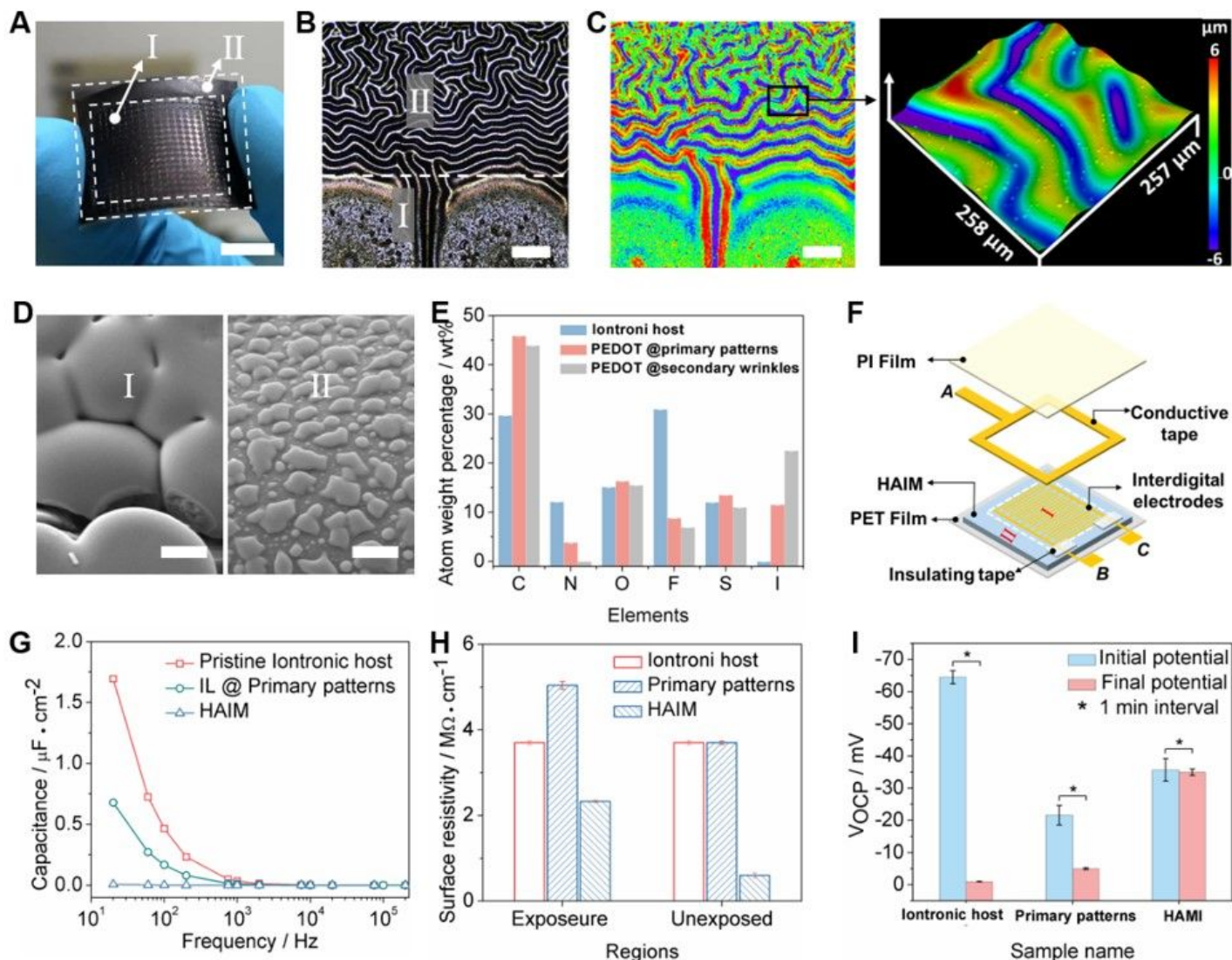


**Figure 5**

Characterization of the ionic electrical performance of HAIM (A) Optical images of the as-prepared HAIM, scale bar: 1 cm. (B-C) The microcopy and LSCM images of HAIM corresponding to (A), scale bar: 200  $\mu\text{m}$ . (D) SEM images of resultant PEDOT in different areas corresponding to (B), scale bar: 2  $\mu\text{m}$ . (E) Atom weight percentages changes of different samples obtained by EDS mapping. (F) Home-made devices for the electrical measurements of different samples in this work. (G) Capacitance change versus frequency for different samples. (H) Surface resistivity comparison of different samples. (I) Potential gradient among different samples.

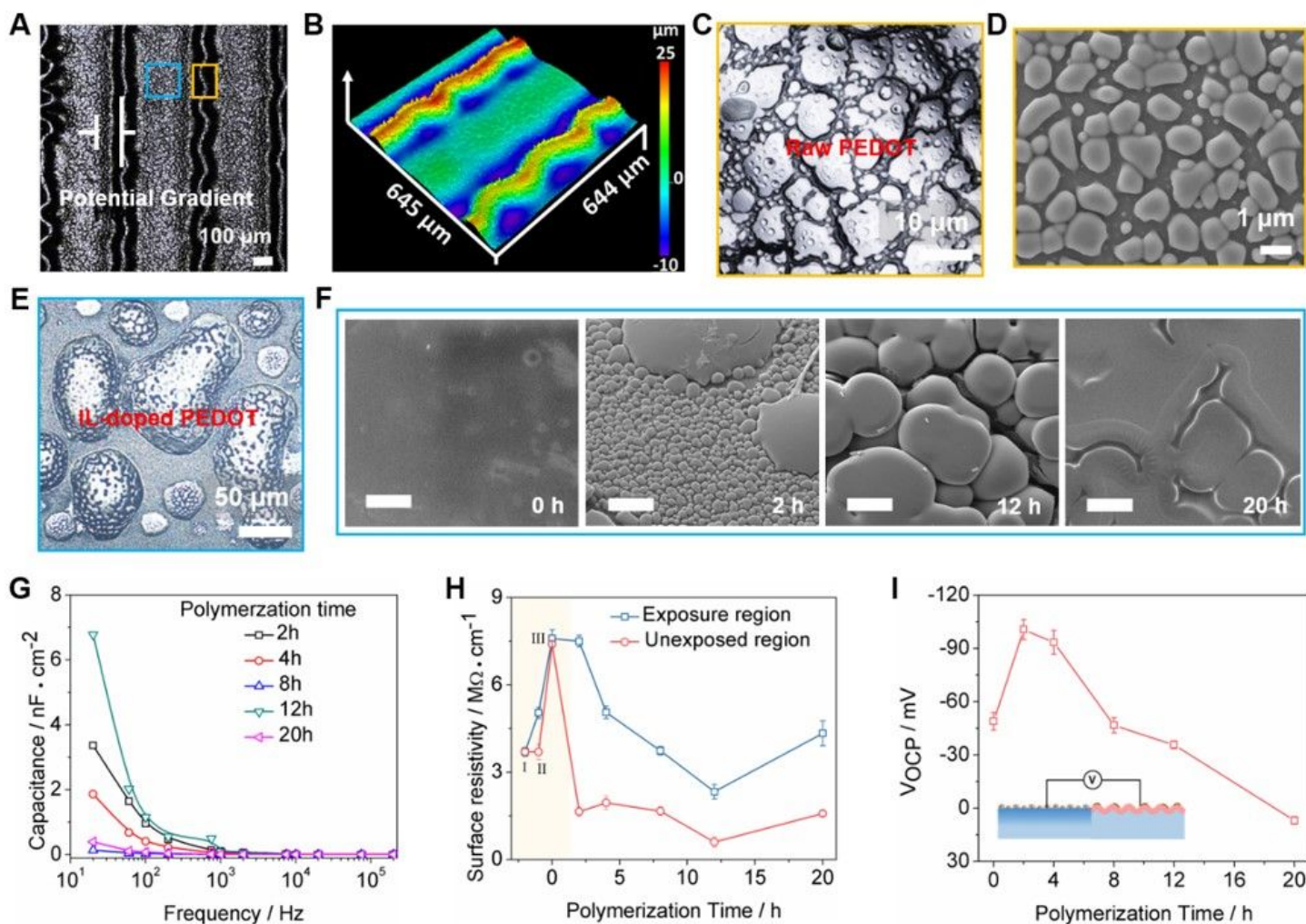


**Figure 6**

Regulation of the potentiometric gradient. (A) Microscopy images of as-prepared stripes HAIM. (B) The LSCM images of the stripes HAIM correspond to (A). (C) Microscopy images and (D) SEM images of raw PEDOT on secondary wrinkles. (E) Microscopy images of as-prepared IL-doped PEDOT after 12 h. (F) The SEM images of IL-doped PEDOT at different polymerization times, scale bar: 5 $\mu\text{m}$ . (G) The interfacial capacitance of as-prepared stripes HAIM versus different polymerization time and frequency. (H) Surface resistivity of as-prepared stripes HAIM under different polymerization times, represents the pristine iontronic host, represents the IL @primary patterns, and represents the IL @primary patterns after absorbing EDOT. (I) The Potentiometric gradient of HAIM against different polymerization times.

## Supplementary Files

This is a list of supplementary files associated with this preprint. Click to download.

- [Supportinginformations.docx](#)